https://doi.org/10.5194/egusphere-2026-3353
Preprint. Discussion started: 7 July 2026

Contrasting physical drivers of chlorophyll-a responses to marine heatwaves in the South China Sea

Yunlu Fang[1,2,3], Cong Liu[1,3], Yicheng Chen[2], Peiliang Li[1,2,3], Mingyang Li[1,2,3]

[1]Hainan Institute, Zhejiang University, Sanya, 572000, China
[2]State Key Laboratory of Ocean Sensing & Ocean College, Zhejiang University, Zhoushan 316021, China
[3]Hainan Provincial Observatory of Ecological Environment and Fishery Resource in Yazhou Bay, Sanya, 572025, China

Correspondence to: Cong Liu (liucong175@gmail.com) and Yicheng Chen (cyc_dsfirst@foxmail.com)

Abstract. In recent years, more frequent marine heatwaves (MHWs) in the South China Sea (SCS) have affected surface chlorophyll-a (Chl-a). Traditional linear statistical methods have limited capacity to identify the contributions of multiple highly interrelated physical drivers in complex oceanic systems. To address this limitation, we applied the Synergistic–Unique–Redundant Decomposition (SURD) method to investigate MHW-related Chl-a anomalies from 1998 to 2024. Analyses reveal a marked regional contrast during summer MHWs, with positive Chl-a anomalies in the northern SCS and negative anomalies in the western SCS. Although summer thermal extremes in both regions were linked to similar anomalous atmospheric circulations associated with the western North Pacific subtropical high, the local physical mechanisms controlling Chl-a responses differed. In the South Vietnam upwelling region, weakened wind forcing reduced Ekman pumping and vertical transport, limiting surface cooling and nutrient replenishment to the euphotic zone, thereby contributing to negative Chl-a anomalies. In the Pearl River Estuary, enhanced incident shortwave radiation promoted rapid surface warming, while weakened wind-driven export favoured the nearshore retention of low-salinity plume water. The SURD results indicate that retained plume water enhanced surface layer stratification and likely increased nutrient supply, allowing plume retention to act synergistically with cumulative heat stress and supporting positive Chl-a anomalies. However, unresolved optical and biological processes in the Pearl River Estuary introduce uncertainty into the inferred nutrient pathway. These results suggest that besides thermal forcing, Chl-a responses to MHWs in marginal seas are also significantly affected by regional physical pathways.

1 Introduction

Under excessive greenhouse gas emissions, the Earth's climate system is experiencing an unprecedented energy imbalance (Robinson et al., 2021; von Schuckmann et al., 2020). As the largest heat sink in the climate system, the ocean has absorbed more than 90 % of the excess heat, contributing to a continued rise in global sea surface temperature (SST) and more frequent marine heatwaves (MHWs) (Cheng et al., 2019). Since the twentieth century, global MHW frequency and mean duration have increased by approximately 34 % and 17 %, respectively (Oliver et al., 2018). As global warming intensifies during the twenty-first century, MHWs are projected to expand nonlinearly in spatial extent and destructive potential (Oliver et al., 2018; Yao et

https://doi.org/10.5194/egusphere-2026-3353
Preprint. Discussion started: 7 July 2026

al., 2020), exerting diverse impacts on the marine biosphere, including shellfish diseases and mollusk mortality (Jones et al., 2018; Oliver et al., 2017), coral reef bleaching (Le Nohaïc et al., 2017), functional extinction of kelp forests (Wernberg et al., 2016), harmful algal blooms, and mass strandings of marine mammals and seabirds (Cavole et al., 2016).

Marine phytoplankton underpin global primary productivity and biogeochemical cycles, and their sensitivity to environmental variability is reflected in variations in chlorophyll a (Chl-a) (Fernández-González et al., 2022). However, the mechanisms by which MHWs influence Chl-a are complex and spatially heterogeneous. In low-latitude waters, MHW-induced thermal stratification can restrict the vertical transport of subsurface nutrients, leading to declines in Chl-a concentrations (Le Grix et al., 2021; Montie et al., 2020; Noh et al., 2022). By contrast, in high-latitude light-limited regions, a shallower mixed layer can enhance phytoplankton blooms by improving light availability within the euphotic zone (Le Grix et al., 2021; Noh et al., 2022). Such spatial variability makes it difficult to generalize or evaluate the ecological impacts of MHWs based on a single physical mechanism.

The South China Sea (SCS), the largest marginal sea in the western Pacific Ocean, is governed by a complex monsoon circulation system and hosts extensive coral reef ecosystems (Li et al., 2011), rendering it highly sensitive to climate change. Observational and reanalysis data identify the SCS as a hotspot for MHWs, with their frequency, duration, and intensity showing significant upward trends (Li et al., 2019; Yao and Wang, 2021). In particular, previous studies have identified the northern SCS continental shelf and the western SCS as active regions of MHW occurrence, with documented regional differences in coastal warming amplitudes and seasonal variability (Wang et al., 2022, 2023). Although previous studies have characterized the spatiotemporal evolution of MHWs in the SCS (Wang et al., 2021), their ecological impacts remain less well understood, partly because of methodological challenges.

Previous studies have documented anomalous Chl-a responses during MHWs in the SCS (Chen et al., 2024; He et al., 2023). However, most attribution analyses still rely on traditional linear statistical methods, such as correlation analysis and multiple linear regression. These methods have inherent limitations when applied to complex marine systems where environmental variables are highly interrelated. In particular, they struggle to disentangle overlapping influences among drivers such as SST, wind fields, and mixed layer depth (MLD), and rarely resolve synergistic effects of these factors. Thus, a key scientific question remains unresolved: are Chl-a anomalies during MHWs mainly driven by direct thermal effects, or by concurrent changes in the physical environment?

To address these limitations, this study applies the Synergistic–Unique–Redundant Decomposition (SURD) method (Martínez-Sánchez et al., 2024). SURD decomposes the information shared between candidate drivers and the target variable into redundant, unique, and synergistic components. This allows us to distinguish independent, overlapping, and joint contributions of physical drivers to Chl-a anomalies during MHWs. By applying this framework to the SCS, this study aims to clarify why Chl-a responses differ among regions and to identify the physical pathways associated with these differences. These results provide a clearer view of regional Chl-a variability during MHWs in the SCS and improve our understanding of physical–biological coupling in marginal seas.

https://doi.org/10.5194/egusphere-2026-3353
Preprint. Discussion started: 7 July 2026

The remainder of this paper is organized as follows. Sect. 2 describes the datasets, MHW identification, Chl-a anomaly analysis, and SURD method. Sect. 3 presents the spatiotemporal characteristics of MHWs in the SCS and the associated Chl-a responses. Sect. 4 examines the regional physical–biological mechanisms in the Vietnam upwelling area and the Pearl River Estuary. Sect. 5 summarizes the main conclusions.

2 Materials and methods

2.1 Study area

The SCS is a semi-enclosed basin whose circulation is governed by the East Asian monsoon system (Jiang et al., 2023). The prevailing southwest winds in summer and northeast winds in winter (Liu and Xie, 1999) drive a seasonally reversing basin-scale circulation and shape a range of complex coastal dynamical processes. In recent years, the region has also become a hotspot for MHWs, posing a growing threat to marine ecosystem stability.

This study focuses on two representative regions within the SCS that exhibit contrasting dynamical characteristics:

The Pearl River Estuary (PRE) and its adjacent waters are located on the northern continental shelf of the SCS (Fig. 1) and represent a typical runoff-dominated estuarine ecosystem. The Pearl River, the second-largest river system in China, delivers substantial summer runoff to the continental shelf, transporting freshwater and terrestrial nutrients (Harrison et al., 2008) that sustain high primary productivity in this region (Ye et al., 2020).

The Vietnam Upwelling Area (VUA) defined in this study is located off southeastern Vietnam and lies within the broader South Vietnam upwelling region (Fig. 1). It represents a principal summer wind-driven upwelling system of the SCS. The strong summer southwest monsoon generates offshore Ekman transport in this region (Ngo and Hsin, 2021), driving the upwelling of cold subsurface water. This process transports nutrient-rich deep water into the euphotic zone, forming a characteristic summer belt of high Chl-a concentration (Liu and Tang, 2022).

https://doi.org/10.5194/egusphere-2026-3353
Preprint. Discussion started: 7 July 2026

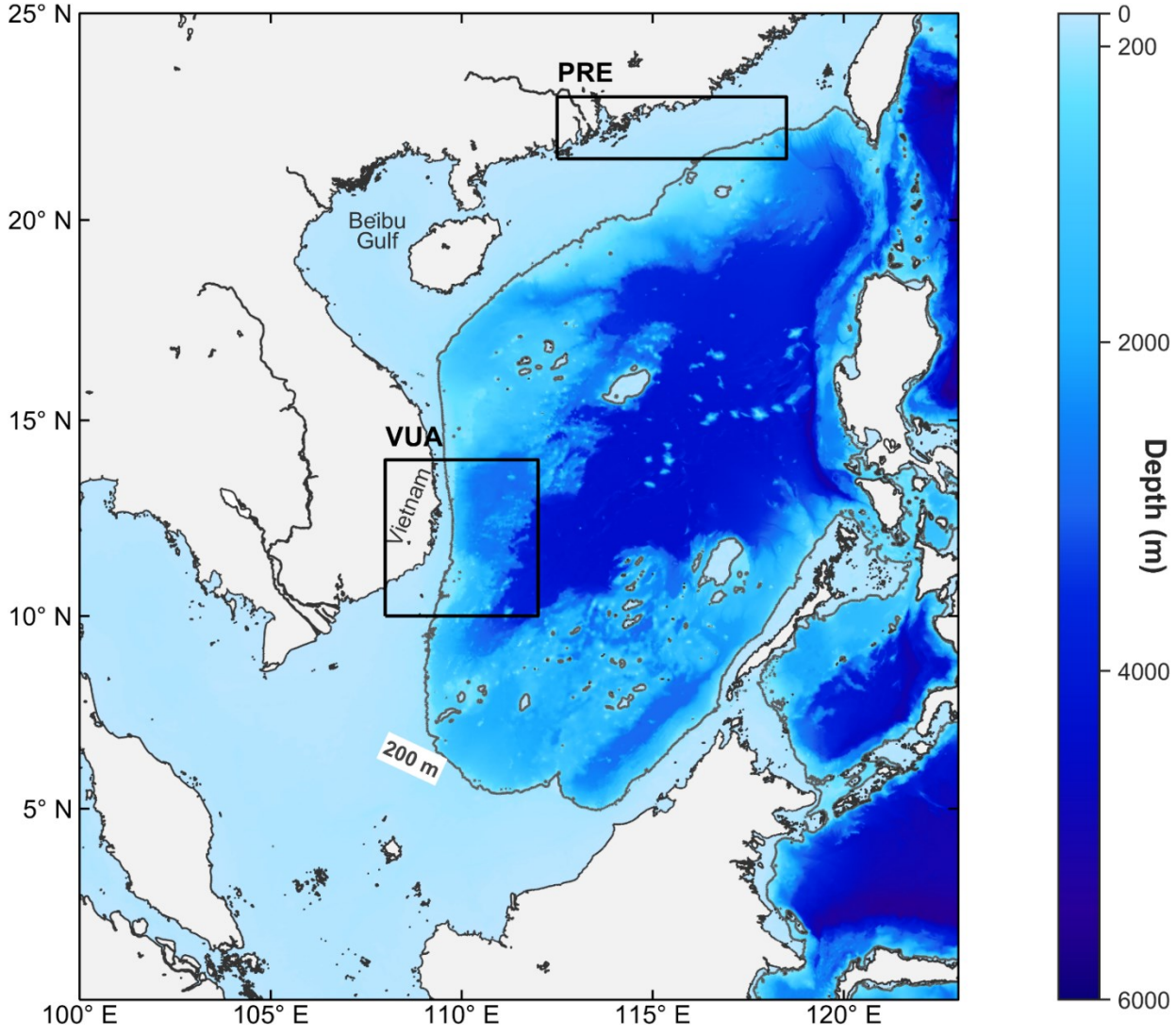

Figure 1. Bathymetry of the South China Sea (SCS) and locations of the two study regions. Shading indicates water depth (m), and the grey contour denotes the 200 m isobath. Black rectangles mark the Pearl River Estuary (PRE) and the Vietnam Upwelling Area (VUA).

2.2 Data sources and preprocessing

A daily dataset covering 1998–2024 was compiled from physical, biological, and atmospheric variables. MHWs were identified using the National Oceanic and Atmospheric Administration (NOAA) Optimum Interpolation Sea Surface Temperature version 2.1 (OISST v2.1) product at 0.25° resolution (Huang et al., 2020), and Chl-a concentrations were obtained from the Copernicus Marine Environment Monitoring Service (CMEMS) GlobColour level 4 (L4) merged product (Global Ocean Colour, 2025). Oceanic physical variables, including sea surface salinity (SSS), MLD, and ocean currents, were obtained from the CMEMS GLORYS12V1 reanalysis, an eddy-resolving product at 1/12° resolution suitable for examining

https://doi.org/10.5194/egusphere-2026-3353
Preprint. Discussion started: 7 July 2026

upper-ocean physical variability (Lellouche et al., 2021; Global Ocean Physics Reanalysis, 2023). Sea level anomaly (SLA) was obtained from the Copernicus Marine Service sea level climate product (Global Ocean Gridded, 2024). The SLA in this product is referenced to the product mean sea surface for 1993–2012, rather than to the 1998–2024 climatology used in this study. Thus, the climatological SLA fields shown later should be interpreted as study-period mean departures from the product reference mean surface. The GlobColour L4 product has also been used in studies of Chl-a variability in the SCS, including analyses of MHW-related Chl-a responses and summer upwelling-associated phytoplankton changes (Liu and Tang, 2022; He et al., 2023). Atmospheric variables were obtained from the European Centre for Medium-Range Weather Forecasts (ECMWF) ERA5 reanalysis. The 10 m winds and surface downward shortwave radiation (SWR) were obtained from ERA5 post-processed daily statistics on single levels (Hersbach et al., 2023b), while 500 hPa geopotential height (GH500) and 850 hPa wind components were obtained from ERA5 post-processed daily statistics on pressure levels (Hersbach et al., 2023a). These atmospheric variables were used to diagnose local wind forcing, radiative forcing during MHWs, and the circulation background related to the western North Pacific subtropical high (WNPSH). Ekman pumping velocity (EPV) was derived from the wind stress curl calculated using ERA5 10 m wind components and was used as an indicator of wind-driven vertical transport. The calculation followed $EPV = (\partial\tau_y/\partial x - \partial\tau_x/\partial y)/(\rho_0 f)$, where τ_x and τ_y are the zonal and meridional wind stress components, ρ_0 is the reference seawater density, and f is the Coriolis parameter.To ensure spatiotemporal consistency among variables for SURD analysis, the OISST grid (0.25° × 0.25°) was adopted as the reference grid, and the remaining datasets were resampled onto this grid using bilinear interpolation. The temporal coverage of all datasets was restricted to 1998–2024, the common period with consistent availability of the key Chl-a, oceanic, and atmospheric variables used in this study. This procedure yielded a unified spatiotemporal dataset for the SURD analysis. Detailed information on the data sources is summarized in Table 1.

Table 1. Summary of the observational and reanalysis datasets.

Category	Variable	Source / Product ID	Temporal resolution	Spatial resolution
Ocean physics	SST	NOAA OISST v2.1	Daily	0.25° × 0.25°
	SSS, currents (u, v), MLD, temperature	CMEMS GLORYS12V1	Daily	1/12° × 1/12°
	SLA	CMEMS SEALEVEL L4	Daily	0.25° × 0.25°
Ocean biology	Chl-a	CMEMS GlobColour L4	Daily	4 km × 4 km
Atmosphere	10 m wind (u, v), SWR	ERA5 single levels	Daily	0.25° × 0.25°
	GH500, 850 hPa wind (u, v)	ERA5 pressure level	Daily	0.25° × 0.25°
Derived variable	EPV	Calculated from ERA5 10 m wind components via wind stress curl	Daily	0.25° × 0.25°

https://doi.org/10.5194/egusphere-2026-3353
Preprint. Discussion started: 7 July 2026

2.3 Research methods

2.3.1 MHW identification and metric calculation

MHW events were identified following the definition of Hobday et al.（2016), using the MATLAB code package developed by Zhao and Marin (2019). Under this framework, MHWs are defined as discrete extreme events characterized by anomalously high SST. The detection criteria were as follows. An MHW event was recorded when daily SST exceeded the seasonally varying 90th percentile threshold for at least five consecutive days. If two events were separated by a gap of two days or less, they were merged into a single event. The period 1982–2011 was used as the climatological baseline for calculating daily thresholds, and detection was applied to SST time series from 1998 to 2024.

Four metrics were calculated at each grid cell to describe the spatial distribution of MHW occurrence and event-scale temporal properties: frequency, duration, total days, and cumulative intensity. MHWs were identified independently from the daily SST time series at each grid cell. Frequency and total days were calculated as the annual number of MHW events and MHW days at each grid cell, respectively, and were then averaged over 1998 to 2024. Duration and cumulative intensity were first calculated for each grid-cell event and were then averaged over all events detected at that grid cell during 1998 to 2024.

2.3.2 SURD causality analysi

To disentangle the causal contributions of environmental drivers to Chl-a anomalies, this study adopted the SURD method. SURD is grounded in information theory and quantifies causality as the reduction in uncertainty (Shannon entropy) of a future target variable provided by the past states of observed drivers. In this study, the target variable Q_j^+ was defined as the Chl-a anomaly at future time $t + \tau$, where τ is the response lag. The observed physical vector $Q = [Q_1, Q_2, \cdots, Q_N]$ represents the states of the selected physical variables at time t. This framework is suitable for the present problem because Chl-a anomalies during MHWs in the SCS are shaped by highly coupled physical drivers and potentially nonlinear interactions. Following the principle of forward information propagation, the total entropy $\mathrm{H}(\mathrm{Q_j^+})$, representing the uncertainty of the future Chl-a anomaly, can be decomposed into redundant, unique, synergistic, and residual components:

$$H(Q_j^+) = \sum_{i \in \mathcal{C}} \Delta I_{i \to j}^{\mathrm{R}} + \sum_{i=1}^{N} \Delta I_{i \to j}^{\mathrm{U}} + \sum_{i \in \mathcal{C}} \Delta I_{i \to j}^{\mathrm{S}} + \Delta I_{\mathrm{leak} \to j} \quad (1)$$

Here, $\mathcal{C}$ denotes the set of all driver combinations involving two or more observed drivers. In the redundant and synergistic sums, $i \in \mathcal{C}$ indexes a driver combination, whereas in the unique term, $i = 1, \ldots, N$ indexes individual drivers. In this study, causality refers to lagged information-theoretic predictive causality under the prescribed driver set and response lag, rather than direct experimental causation. The unique causality ΔI^{U} quantifies the causal information provided by a single driver that is not contained in any other individual driver, thus serving as a key indicator for identifying independent drivers. The redundant causality ΔI^{R} represents the overlapping information arising from shared dependencies among drivers. By separating this shared information, SURD reduces misattribution caused by multicollinearity in traditional models (Han et al.,

https://doi.org/10.5194/egusphere-2026-3353
Preprint. Discussion started: 7 July 2026

2025), preventing correlated signals from being interpreted as independent mechanisms. The synergistic causality ΔI^{S} represents causal information about future Chl-a anomalies that can be obtained only from the joint states of multiple selected physical drivers, rather than from any single driver alone. It therefore indicates additional information on the future Chl-a response arising from interactions among the selected drivers. The causality leak ΔI_{leak} quantifies target uncertainty not assigned to the selected driver set under the prescribed lag, variable subset, and discretization scheme. It may reflect unresolved processes, observational uncertainty, finite-sample effects, or missing variables.

In practice, SURD requires the estimation of the joint probability distribution between the future Chl-a anomaly and the selected physical drivers. Given the continuous nature of these anomalous time series, they were first discretized into a finite number of states before estimating the joint probability distribution. The number of bins defines the number of discrete states used to represent each variable and therefore controls the resolution of the discretized state space. Too few bins may merge distinct anomaly states and obscure variability, whereas too many bins may leave insufficient samples in each state and lead to unstable probability estimates. We tested bin numbers from 2 to 10 and selected the final bin number based on a low causality leak and stable dominant contribution patterns. The lag τ defines the time interval between the past physical drivers and the future Chl-a anomaly. Lag sensitivity tests were conducted for τ = 1, 2, and 3 days to examine whether the main SURD contribution rankings were sensitive to the assumed response lag. Because the dominant rankings were stable across these tested lags, τ = 1 day and nine bins were retained for the main analysis.

The non-leak SURD terms were normalized by the mutual information captured by the selected driver subset. Therefore, for a given non-leak term k, the percentage shown in Figs. 5b and 8b was calculated as

$$P_k = 100 \times \frac{\Delta I_k}{\sum_{\ell \in \Omega} \Delta I_\ell} \tag{2}$$

where Ω includes all unique, redundant, and synergistic terms of the selected driver subset, but excludes the causality leak. These percentages therefore represent relative information contributions within the information captured by the selected physical drivers. They should not be interpreted as fractions of total Chl-a variance or total target entropy. The causality leak is reported separately because it is normalized by $\mathrm{H}(\mathrm{Q}_{\mathrm{j}}^{+})$ and measures the fraction of target uncertainty that remains unexplained by the selected driver set.

3 Results

3.1 Spatial distribution of MHWs

MHW metrics in the SCS exhibit marked spatial heterogeneity (Fig. 2). In terms of occurrence frequency (Fig. 2a), high values are mainly concentrated on the northern continental shelf, with annual occurrence frequencies generally exceeding 4 events year^{-1}. High values of single-event duration (Fig. 2b) and cumulative intensity (Fig. 2d) are present in the Beibu Gulf, off Vietnam, and in the western SCS basin, where the mean duration exceeds 15 days. Annual total MHW days display a spatial pattern characterized by higher values in coastal regions and lower values in the open basin (Fig. 2c). In the Beibu Gulf and

https://doi.org/10.5194/egusphere-2026-3353
Preprint. Discussion started: 7 July 2026

PRE, annual total MHW days exceed 50 days. These patterns indicate pronounced MHW activity in the northern shelf region, including the PRE, and in the VUA.

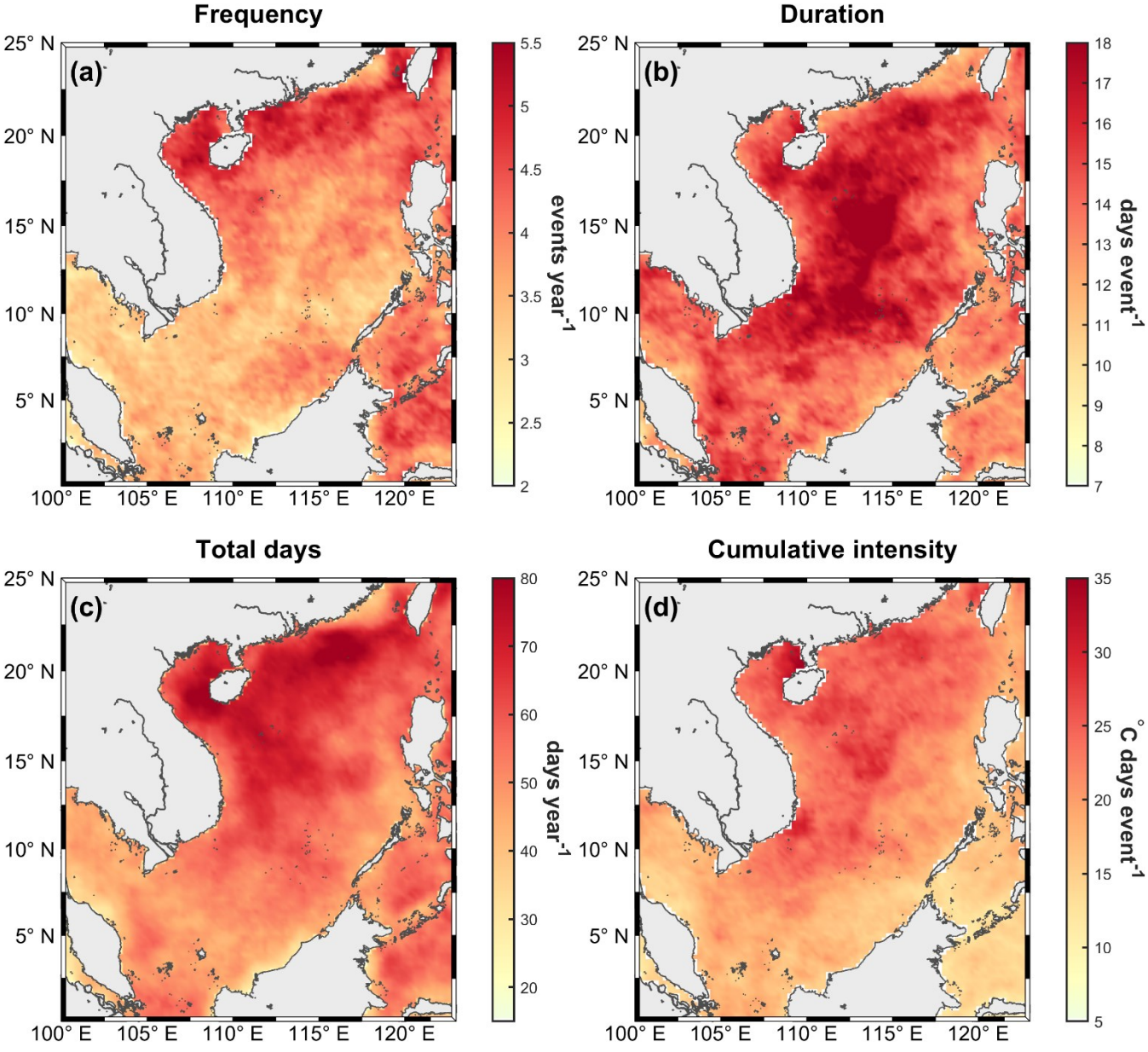

Figure 2. Mean spatial distribution of MHW characteristics in the SCS during 1998 to 2024. The panels show (a) annual mean occurrence frequency (events year⁻¹), (b) mean duration (days event⁻¹), (c) annual mean total MHW days (days year⁻¹), and (d) annual mean cumulative intensity (°C days event⁻¹).

Statistical analyses further quantified the MHW characteristics of the VUA and the PRE relative to the basin-wide SCS statistics ($p < 0.01$; Fig. 3). The PRE is characterized as a typical high-frequency area. The annual occurrence frequency ranges from 3.41 to 5.37 events year⁻¹, with a median of 4.57 events year⁻¹, which is higher than the basin-wide SCS median of 3.78

https://doi.org/10.5194/egusphere-2026-3353
Preprint. Discussion started: 7 July 2026

events year^{-1} (Fig. 3a). The VUA, by comparison, is characterized as a long-duration area. In this region, the median duration of individual events reaches 16.63 days event^{-1}, exceeding the basin-wide SCS median of 14.30 days event^{-1} (Fig. 3b). In addition, both the PRE and the VUA exhibit higher median annual total MHW days and cumulative intensity than the basin-wide SCS median values (Fig. 3c, d).

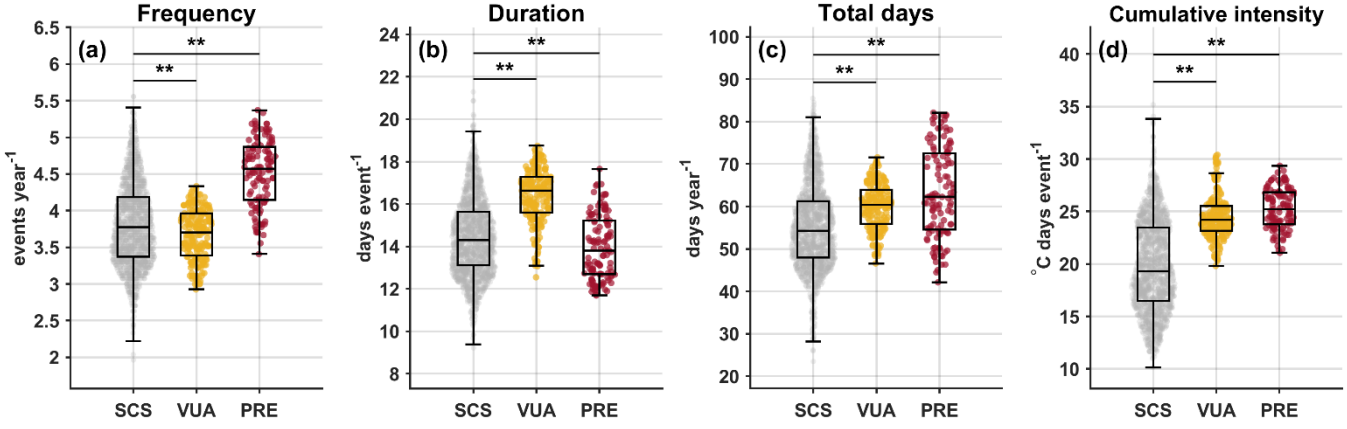

Figure 3. Comparison of MHW characteristics among the SCS, the VUA, and the PRE. The panels show (a) annual mean occurrence frequency, (b) mean duration, (c) annual mean total MHW days, and (d) annual mean cumulative intensity. Each point represents one valid grid cell, with values averaged over 1998 to 2024. Boxes indicate the interquartile ranges, and central horizontal lines denote medians. Horizontal bars indicate comparisons of VUA versus SCS and PRE versus SCS; double asterisks indicate significant differences based on two-sided Wilcoxon rank-sum tests (Wilcoxon, 1945; **, $p < 0.01$).

3.2 Chl-a responses to MHWs

Seasonal composite analysis of Chl-a anomalies during MHWs reveals a predominantly negative response across most seasons (Fig. 4). In spring, autumn, and winter, negative Chl-a anomalies dominate the SCS (Fig. 4a, c, d). By contrast, the summer response exhibits a marked spatial contrast between the northern shelf and the western SCS (Fig. 4b). In the PRE and adjacent northern shelf regions, Chl-a concentrations show positive anomalies during MHWs, with increases exceeding 40 % in some nearshore core areas. Meanwhile, the VUA shows negative Chl-a anomalies. The following sections therefore focus on the PRE and VUA, which represent coherent positive and negative summer anomaly centres, to examine the coupled processes underlying these contrasting responses.

https://doi.org/10.5194/egusphere-2026-3353
Preprint. Discussion started: 7 July 2026

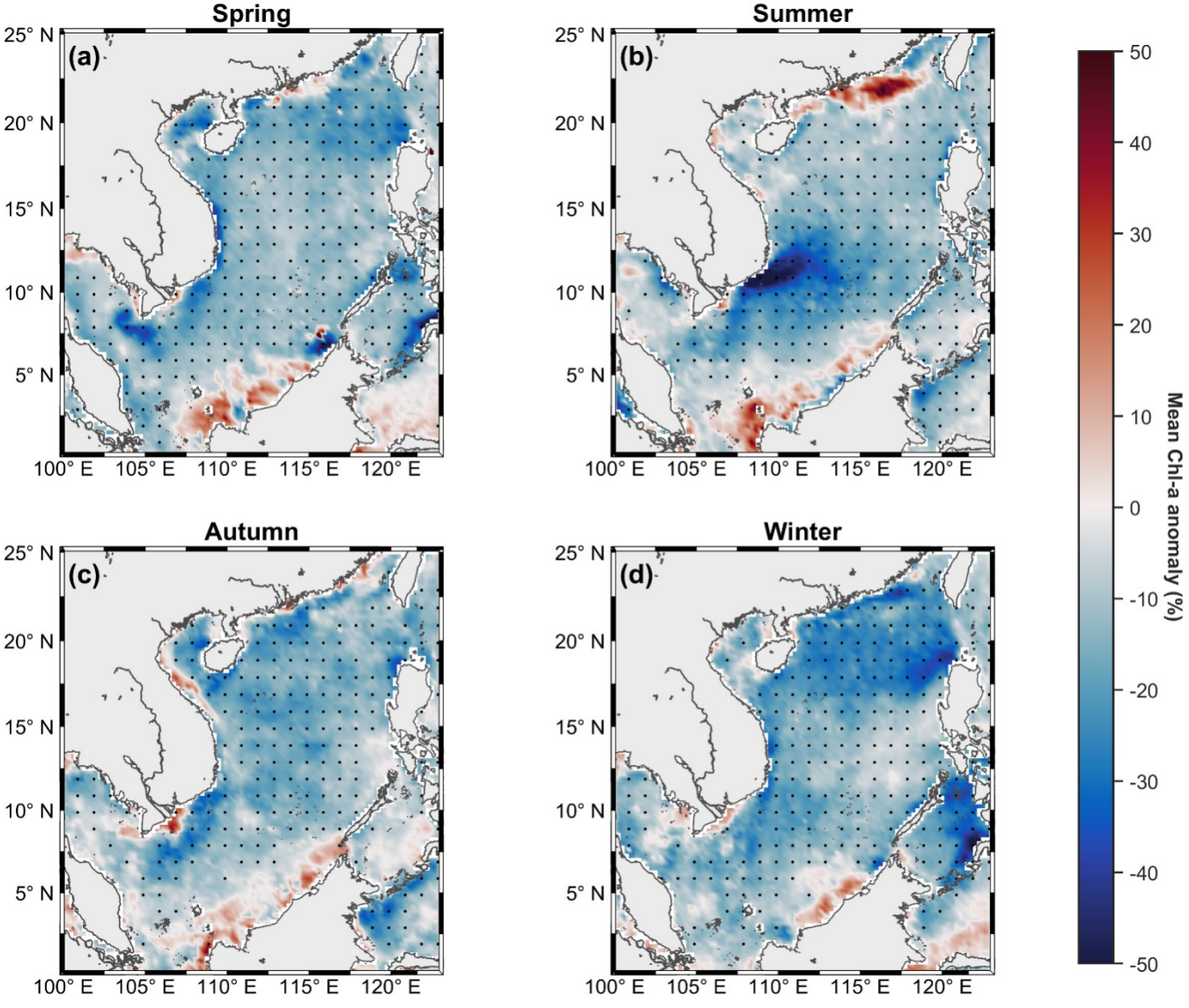

Figure 4. Spatial distribution of the seasonal mean Chl-a percentage anomalies during MHWs in the SCS for 1998 to 2024. The panels show composite anomalies for (a) spring, (b) summer, (c) autumn, and (d) winter. Chl-a anomalies are expressed as percentage differences between event-mean values during MHWs and the seasonal climatology at each grid cell. Black stippling indicates anomalies significantly different from zero ($p < 0.05$).

4 Regional physical pathways of Chl-a responses during MHWs

4.1 SURD-based attribution of regional physical drivers

To identify the dominant physical signals associated with summer Chl-a anomalies during MHWs across different regions, we applied SURD for causal attribution analysis. Cumulative SST intensity (SST_CUM) was used as the core thermal-stress

https://doi.org/10.5194/egusphere-2026-3353
Preprint. Discussion started: 7 July 2026

metric and was retained in all tested variable subsets. This design allowed us to evaluate whether Chl-a anomalies during MHWs were mainly associated with cumulative heat stress itself or with concurrent changes in other physical processes. For each region, three additional variables were combined with SST_CUM from the remaining candidate pool: SSS, SLA, MLD, EPV, zonal and meridional current components, wind speed, and zonal (u_wind) and meridional (v_wind) wind components. These variables cover key physical pathways known to regulate Chl-a variability in the SCS, including monsoon wind forcing, Ekman pumping, coastal and offshore circulation, mesoscale modulation, and upper-ocean thermohaline structure (Lu and Gan, 2015; Chen et al., 2021; Hong et al., 2022; Zhi et al., 2022). Nutrient and biological variables were not included in the SURD driver pool because daily, spatially continuous, and regionally consistent datasets for these variables are not available with sufficient reliability over 1998 to 2024 for both study regions. This limitation is important in nearshore and estuarine waters, where optically complex water affects satellite retrievals and model-derived biogeochemical variables are subject to uncertainties related to parameterization and limited observational constraints (Aurin and Dierssen, 2012; Mamnun et al., 2022; Skákala et al., 2024). We therefore constrained the main SURD analysis to physical variables from mature satellite and reanalysis products, while treating unresolved nutrient, optical, and biological processes as sources of causality leak in Sect. 4.3. Adding more variables can reduce the causality leak in principle because the future Chl-a state is conditioned on a larger set of drivers. However, a lower leak alone does not necessarily indicate a more physically interpretable driver set. We therefore used four-variable subsets as a parsimonious setting that balances leak reduction, probability-estimation stability, and mechanistic interpretability. This choice also avoids an overly high-dimensional joint probability space and higher-order SURD terms that are difficult to relate to specific physical processes. Within this constrained framework, the selected subset was the four-variable combination with the lowest mean causality leak over the tested bin numbers. As defined in Sect. 2.3.2, the SURD contribution percentages reported below refer to non-leak terms normalized within the mutual information captured by each selected variable subset. The causality leak is normalized separately and is shown independently.

4.1.1 Suppressed upwelling in the VUA

As a typical wind-driven upwelling system, the VUA is strongly regulated by local air–sea interactions during summer (Ngo and Hsin, 2021). Within the tested four-variable subsets described above, the combination of SSS, SLA, EPV, and SST_CUM had the lowest mean causality leak over the tested bin numbers, with a leak of approximately 0.55 under the selected nine-bin discretization (Fig. 5a). This subset was therefore used to examine the physical information associated with VUA Chl-a anomalies.

Figure 6 illustrates climatological fields and MHW-related composite anomalies for key variables in the VUA during summer. The climatological fields show the canonical summer upwelling signature off southeastern Vietnam, including relatively lower SST, enhanced EPV, lower nearshore SLA, and a nearshore high-Chl-a belt (Fig. 6a, b, d, e). This pattern agrees with previous studies indicating that southwest monsoon forcing and Ekman processes drive coastal and offshore upwelling in the western SCS, thereby supporting elevated Chl-a in the upwelling zone (Herrmann et al., 2023; To Duy et al., 2022; Zhao and Tang, 2007).

https://doi.org/10.5194/egusphere-2026-3353
Preprint. Discussion started: 7 July 2026

Elevated SST_CUM values span the entire region, with high-value centres (>30 °C days) concentrated in offshore waters and along the nearshore band south of 12° N (Fig. 6f). Correspondingly, Chl-a concentrations show negative anomalies (Fig. 6j), with the core decline zone (10 to 12° N) overlapping the coastal region experiencing the strongest cumulative heat stress. These negative Chl-a anomalies spatially coincide with the summer climatological high-Chl-a belt (Fig. 6e), suggesting that MHWs suppress productivity in a climatologically productive area.

These negative Chl-a anomalies cannot be solely explained by direct surface warming. As indicated by the SURD analysis (Fig. 5b), among the individual variables, EPV provides the largest unique information contribution (12.9 %). This result identifies vertical transport as the primary independent physical driver of the Chl-a decline within the selected variable set. EPV exhibits negative anomalies along the coast, with a spatial extent that generally coincides with the core region of negative Chl-a anomalies (Fig. 6g, j). This phenomenon further supports that negative EPV anomalies contribute to the Chl-a decline.

Substantial redundant information is shared by SSS and EPV (18.9 %; Fig. 5b), consistent with the spatial overlap of their negative anomalies (Fig. 6g, h). This redundancy suggests that SSS variability contains information linked to EPV. Reduced EPV suppresses the upward transport of subsurface high-salinity water, contributing to surface freshening (Ngo and Hsin, 2021; To Duy et al., 2022). Thus, the negative SSS anomaly can be interpreted as a hydrographic tracer of weakened wind-driven upwelling (Dippner et al., 2007; Wu et al., 2025).

Within the explainable information captured by the selected subset, the largest single contribution (20.9 %) arises from the synergistic interaction among SSS, SLA, EPV, and SST_CUM. Given SURD terms are not stepwise marginal effects, the four-variable synergy should not be interpreted as the incremental effect of adding SSS to a lower-order combination. The SSS–EPV redundancy mainly reflects shared upwelling-related information. The dominant four-variable synergy therefore supports a joint-state interpretation rather than a single-driver explanation. The vertical structure further supports this point (Fig. 7). During MHWs, positive temperature anomalies penetrate into the subsurface layer (Fig. 7f), strengthening water-column stratification, as reflected by positive N^2 anomalies (Fig. 7i). N^2 denotes the squared Brunt–Väisälä frequency, which was estimated from the vertical density gradient derived from the temperature and salinity sections. Positive SLA anomalies (Fig. 6i) correspond to thermocline deepening (Fig. 7e, f), while negative EPV anomalies indicate weakened upwelling. This synergy can be interpreted as a dual suppression mechanism: dynamically, reduced wind-driven upwelling limits the upward transport of nutrients (He and Mahadevan, 2021); thermally, enhanced stratification further restricts vertical nutrient exchange in the upper ocean (Yao and Wang, 2021; Noh et al., 2022). Together, these processes reduce nutrient replenishment to the euphotic zone and ultimately suppress phytoplankton biomass (He et al., 2023; Ma and Chen, 2025).

https://doi.org/10.5194/egusphere-2026-3353
Preprint. Discussion started: 7 July 2026

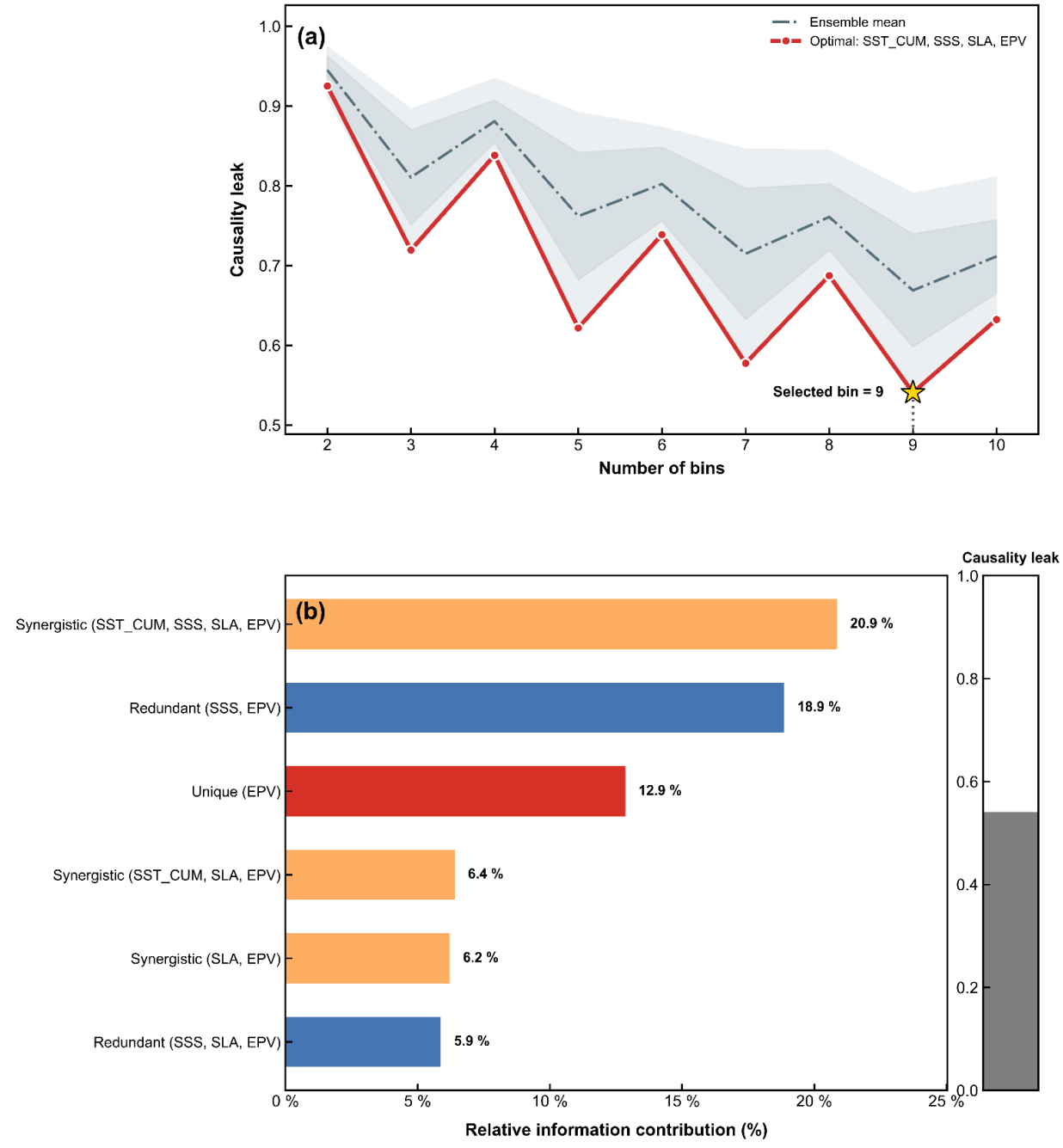

Figure 5. Selection of the four-variable subset and SURD decomposition for the VUA during summer MHWs (a) Sensitivity of the causality leak to the number of bins. The solid red line denotes the selected variable subset, and the dot-dashed grey line denotes the ensemble mean across all four-variable subsets. Shading indicates the full range and ±1 standard deviation of the ensemble. The yellow star marks the selected discretization parameter of nine bins. (b) Relative non-leak information contributions to the future Chl-a anomaly. Percentages are normalized by the sum of all unique, redundant, and synergistic SURD terms for the selected subset. The grey bar indicates the causality leak, $\Delta I_{\mathrm{leak}\to j}/H(Q_j^+)$, which is normalized separately. Only the six largest non-leak terms are shown; therefore, the displayed percentages do not sum to 100 %.

https://doi.org/10.5194/egusphere-2026-3353
Preprint. Discussion started: 7 July 2026

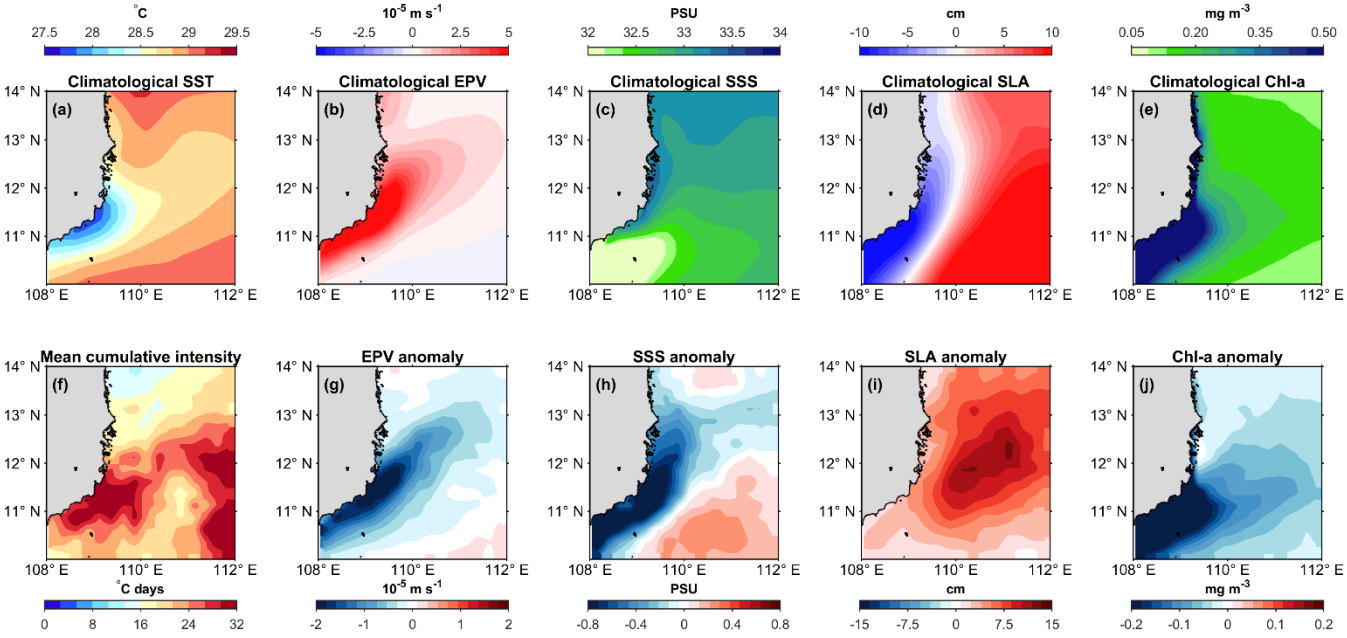

Figure 6. Summer climatological fields and MHW-related anomaly composites in the VUA. Panels show (a) climatological SST (°C), (f) mean cumulative intensity of summer MHWs (°C days), and climatological fields with corresponding anomaly composites for (b, g) EPV (10^{-5} m s^{-1}), (c, h) SSS (PSU), (d, i) SLA (cm), and (e, j) Chl-a (mg m^{-3}). The anomaly fields were calculated from daily departures relative to the day-of-year climatology and then averaged using an event-equal composite.

https://doi.org/10.5194/egusphere-2026-3353
Preprint. Discussion started: 7 July 2026

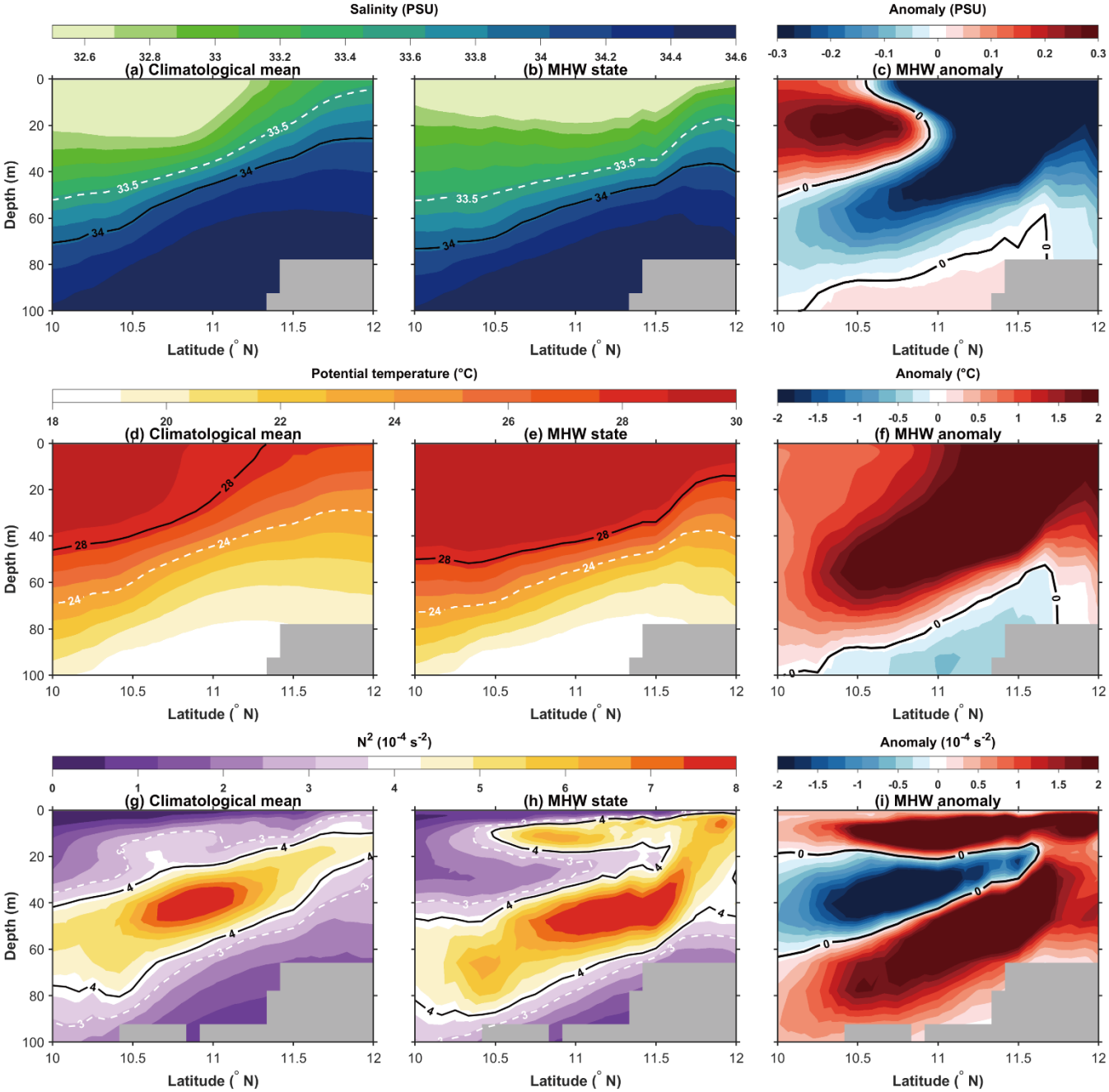

Figure 7. Vertical upper-ocean structure (0 to 100 m) along the 109.33° E transect in the VUA during summer (June to August). The rows display, from top to bottom, the (a–c) salinity (PSU), (d–f) potential temperature (°C), and (g–i) squared Brunt–Väisälä frequency (N^2, 10^{-4} s^{-2}). The left, middle, and right columns represent the climatological mean, MHW state, and MHW anomaly field, respectively. In the left and middle columns, solid black and dashed white contours indicate selected salinity, potential-temperature, and N^2 values. In the right column, thick black contours denote zero anomalies. Grey shading at the bottom of each panel represents seafloor bathymetry.

https://doi.org/10.5194/egusphere-2026-3353
Preprint. Discussion started: 7 July 2026

4.1.2 Horizontal plume retention in the PRE

Using the same four-variable selection framework as in the VUA, the PRE subset selected at the nine-bin discretization consisted of SSS, SLA, SST_CUM, and u_wind (Fig. 8a). Although the causality leak continued to decrease at 10 bins, nine bins were retained for the main analysis to maintain comparability with the VUA and to avoid excessive sparsity in the discretized joint probability estimates. Within this selected subset, the largest non-leak contribution was the four-variable synergistic term involving SST_CUM, SSS, SLA, and u_wind (30.6 %; Fig. 8b). SST_CUM had a negligible unique contribution, indicating that cumulative heat stress provided little independent information on the positive Chl-a anomalies within the selected physical-variable framework. Instead, SSS provided the largest unique information contribution within the explainable component captured by the selected subset (28.1 %; Fig. 8b), pointing to plume-related hydrographic variability as the key independent signal. This interpretation is supported by the spatial pattern of SSS. The climatology shows low-salinity plume water near the estuary and more saline offshore waters (Fig. 9e), while the MHW composite exhibits positive SSS anomalies dominating the area outside the plume-affected region (Fig. 9f). Therefore, the intrusion of high-salinity offshore waters—both climatological and anomalous—cannot account for the pronounced negative SSS anomalies in the nearshore area (Fig. 9f). In addition, the pronounced negative SSS anomalies were mainly concentrated in the plume-affected region (Fig. 9e, f). These results suggest that the nearshore freshening is caused by the enhanced influence or local retention of low-salinity Pearl River plume water. In the eutrophic PRE, where nutrient concentrations often exhibit a negative correlation with salinity (Dai et al., 2008; Niu et al., 2020), this low-salinity signal supports the interpretation that nutrient-rich plume water was retained near the coast, providing favourable conditions for positive Chl-a anomalies. The same low-salinity surface layer can also reduce surface density and strengthen salinity-driven stratification, as supported by the salinity and N^2 anomaly sections in Fig. S1a and c in the Supplement.

The four-variable synergy among SST_CUM, SSS, SLA, and u_wind supports a joint-state interpretation rather than a single-driver response. This term should not be interpreted as the sum of separate marginal effects from u_wind and SLA. The negligible unique contributions of u_wind and SLA indicate that neither variable provides strong independent information on themselves. Instead, they become informative in the joint state because they help distinguish plume-retention conditions during cumulative heat stress. The composite fields show weakened winds relative to the summer monsoon background (Fig. 9c, d), reducing wind-driven offshore Ekman transport and favouring nearshore plume retention. Positive SLA anomalies over the adjacent shelf suggest elevated nearshore sea level during MHWs (Fig. 9h). This sea-level rise would reduce the estuary–shelf water-level gradient and slow the offshore spreading of plume water, reinforcing the retention effect of weakened winds. Sustained surface heating could further stabilize the upper layer, as indicated by positive temperature and N^2 anomalies in Fig. S1b and c in the Supplement. This stratified surface layer would help maintain nutrient-rich plume water within the euphotic zone. Under these nutrient-rich and stratified conditions, elevated temperatures can favour Chl-a accumulation by enhancing phytoplankton growth rates (Marañón et al., 2018), and extreme temperatures in eutrophic coastal waters have been shown to promote rather than inhibit phytoplankton blooms (Hayashida et al., 2020). Although the selected physical variables support

https://doi.org/10.5194/egusphere-2026-3353
Preprint. Discussion started: 7 July 2026

the plume-retention interpretation, the relatively high causality leak in the PRE indicates that unresolved biogeochemical processes may also contribute to local Chl-a variability.

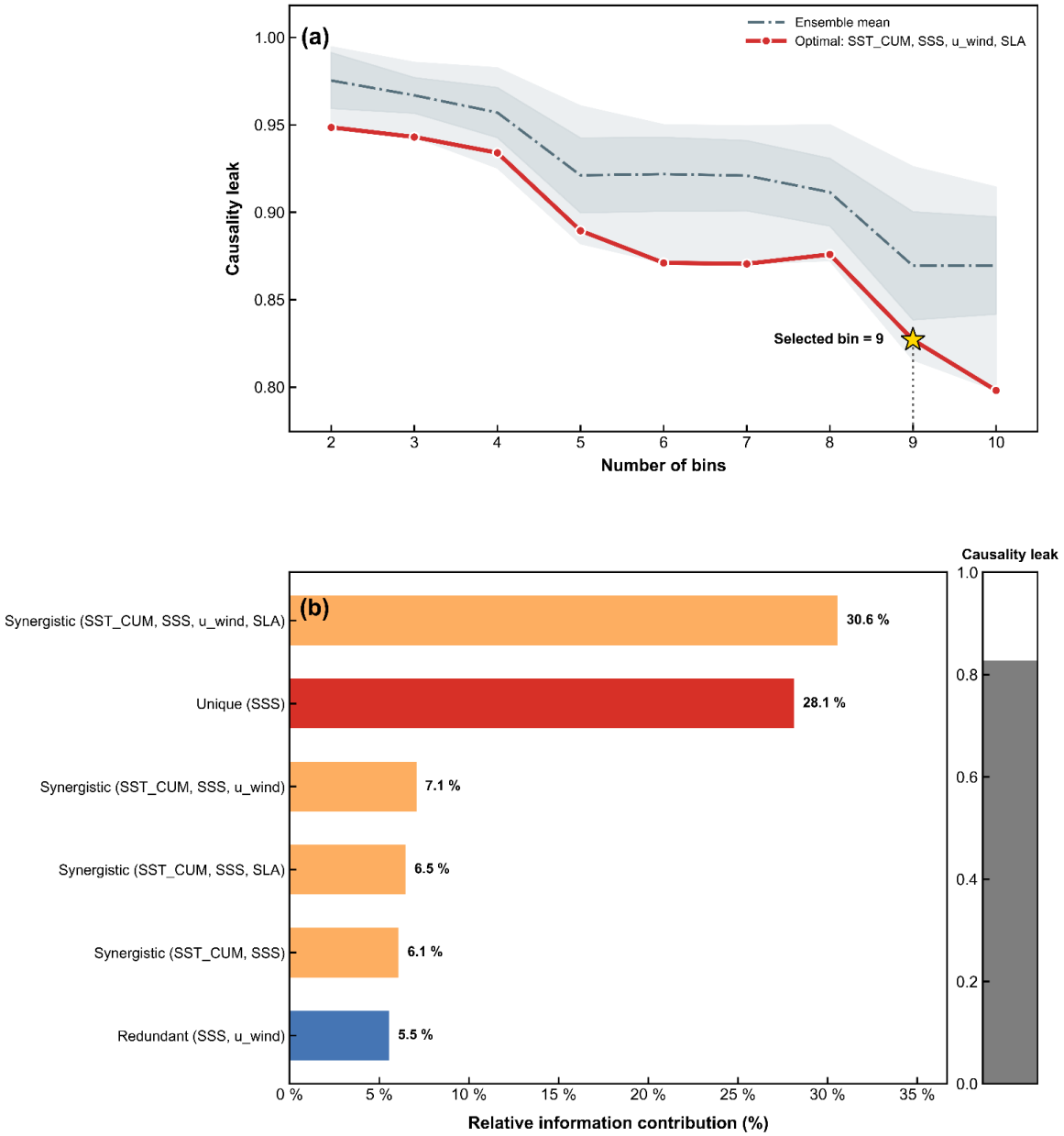

Figure 8. Selection of the four-variable subset and SURD decomposition for the PRE during summer MHWs (a) Sensitivity of the causality leak to the number of bins. The solid red line denotes the selected variable subset, and the dot-dashed grey line denotes the ensemble mean across all four-variable subsets. Shading indicates the full range and ±1 standard deviation of the ensemble. The yellow star marks the selected discretization parameter of nine bins. (b) Relative non-leak information contributions to the future Chl-a anomaly. Percentages are normalized by the sum of all unique, redundant, and synergistic SURD terms for the selected subset. The grey bar indicates the causality leak, $\Delta I_{\mathrm{leak}\to j}/H(Q_j^+)$, which is normalized separately. Only the six largest non-leak terms are shown; therefore, the displayed percentages do not sum to 100 %.

https://doi.org/10.5194/egusphere-2026-3353
Preprint. Discussion started: 7 July 2026

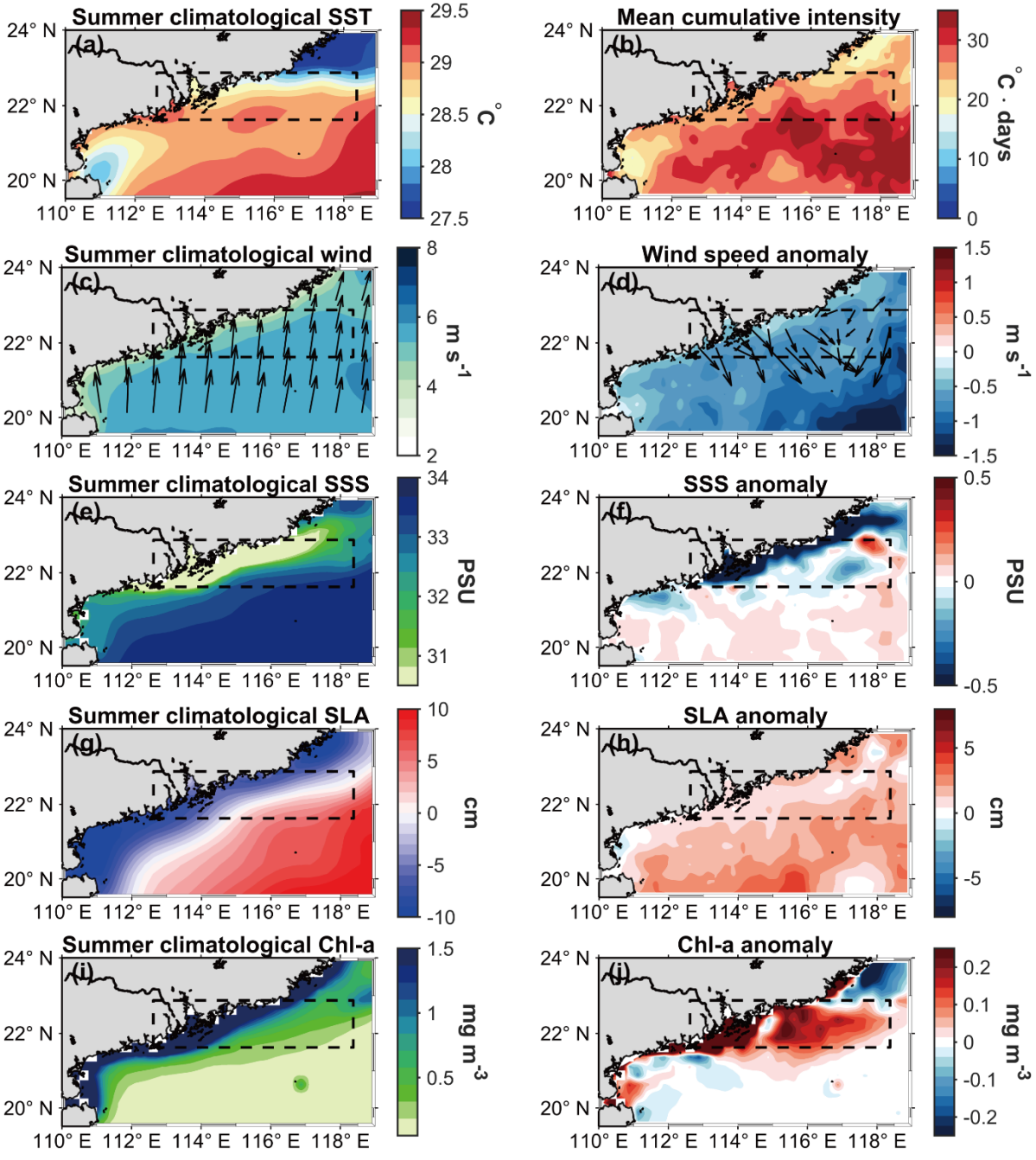

Figure 9. Summer climatological fields and MHW-related anomaly composites in the PRE. The first row shows (a) summer climatological SST (°C) and (b) mean cumulative intensity of summer MHWs (°C days). The remaining rows display, from top to bottom, wind speed (m s⁻¹), SSS (PSU), SLA (cm), and Chl-a (mg m⁻³); the left and right columns represent the summer climatological mean and the corresponding MHW anomaly field, respectively. In the wind panels, arrows indicate climatological wind vectors in (c) and wind-vector anomalies in (d). The dashed black box denotes the PRE region used for regional analysis. The anomaly fields were calculated from daily departures relative to the day-of-year climatology and then averaged using an event-equal composite.

https://doi.org/10.5194/egusphere-2026-3353
Preprint. Discussion started: 7 July 2026

4.2 Contrasting regional responses to the western North Pacific subtropical high

The VUA and the PRE exhibit contrasting Chl-a responses during summer MHWs, yet their respective event composites point to a similar large-scale atmospheric background associated with the westward extension and intensification of the western North Pacific subtropical high (WNPSH; Fig. 10a, b). Here, GH500 denotes 500 hPa geopotential height, expressed in geopotential metres (gpm), and the 5875 gpm contour is used as a proxy for the WNPSH extent (Basconcillo and Moon, 2022; Nie et al., 2024). Under similar large-scale circulation anomalies, differences in regional oceanographic settings give rise to distinct physical pathways and contrasting physical–biological coupling mechanisms (Fig. 11).

In the VUA, MHW occurrence and negative Chl-a anomalies are linked through a common physical pathway. For the VUA events, positive GH500 anomalies and the westward extension of the 5875 gpm contour are accompanied by anomalous low-level winds consistent with weakened southwest monsoon forcing (Yao and Wang, 2021; Li et al., 2022). This shift in dynamical forcing weakens coastal Ekman transport and EPV. This suppression produces two linked effects: first, reduced upwelling of cold subsurface water weakens surface cooling and favours elevated temperatures (Yao and Wang, 2021); second, restricted upward nutrient transport to the euphotic zone decreases Chl-a concentrations. These results indicate that MHW development and reduced Chl-a in the VUA represent coupled thermal and biological responses to weakened vertical dynamics under the same anomalous wind forcing.

By contrast, the PRE exhibits a more complex response, reflecting the joint effects of thermal and dynamical processes. The WNPSH-related anomalies influence the PRE through two distinct pathways. Thermally, the PRE composite shows positive SWR anomalies over the northern shelf (Fig. 10c), indicating enhanced incident shortwave radiation during MHWs. Given that the SST variability in shallow areas is highly sensitive to surface heat fluxes, the enhanced radiation favours rapid surface warming and hence MHW development (Wang et al., 2022; Gao et al., 2023; Chen et al., 2025). Dynamically, WNPSH-related anomalous atmospheric circulations weakened low-level wind forcing over the northern SCS shelf (Fig. 10b), reducing wind-driven offshore transport. As a result, low-salinity river plume water is more likely to be retained nearshore, as reflected by negative SSS anomalies in the plume-affected region (Fig. 9f). In the eutrophic PRE, this retained plume water likely supplied nutrient-rich conditions that favoured positive Chl-a anomalies. These coupled pathways explain the simultaneous occurrence of elevated temperatures and positive Chl-a anomalies in the PRE, linking radiative warming with wind-regulated plume retention and inferred nutrient support.

https://doi.org/10.5194/egusphere-2026-3353
Preprint. Discussion started: 7 July 2026

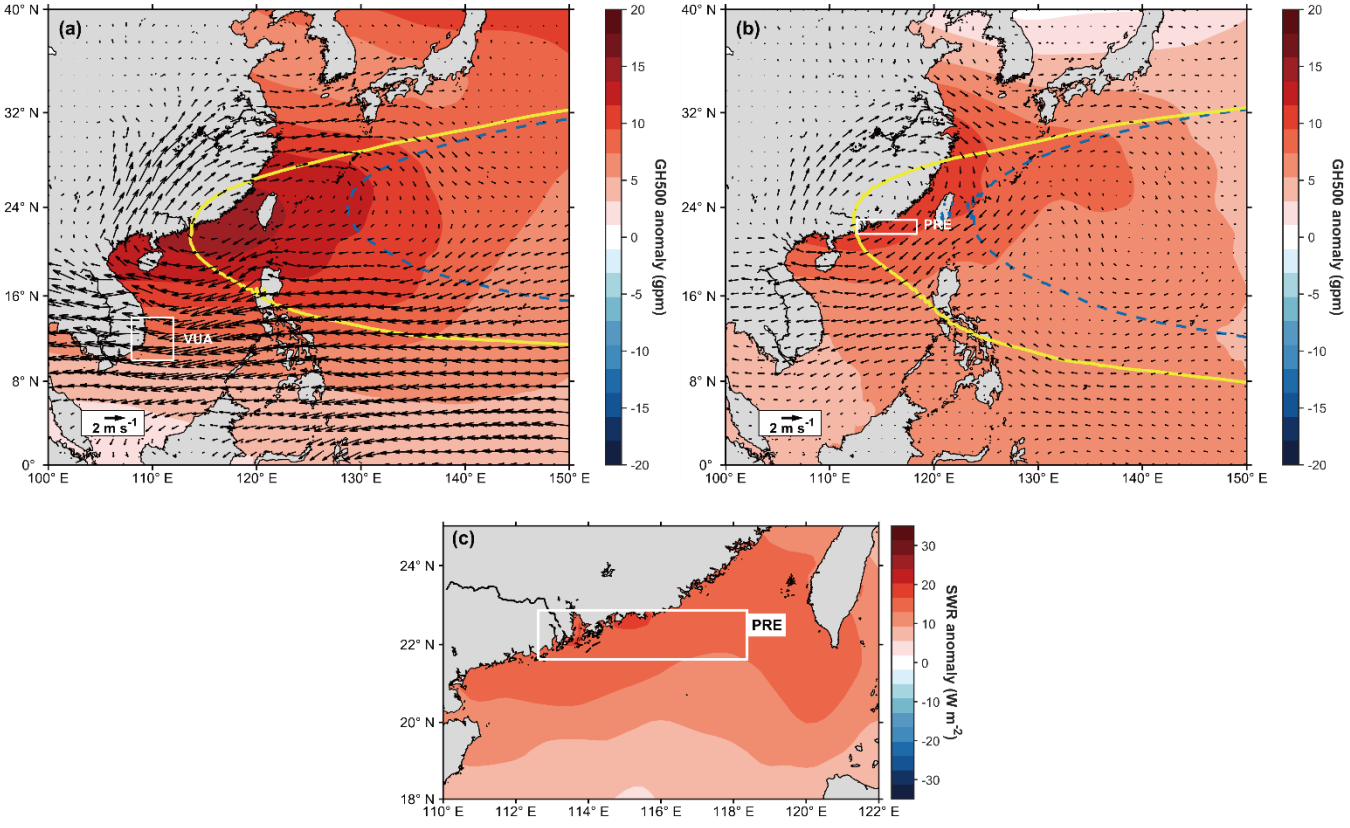

Figure 10. Composite large-scale atmospheric circulation and local shortwave-radiation anomalies during summer MHWs. (a, b) Composite anomalies of 500 hPa geopotential height (GH500; geopotential metres, gpm) and 850 hPa wind (m s^{-1}) for summer MHW events in (a) the VUA and (b) the PRE during 1998 to 2024. The reference vector in panels (a) and (b) indicates 2 m s^{-1}. The dashed blue and solid yellow contours denote the summer-climatological and MHW composite 5875 gpm GH500 contours, respectively. (c) Composite SWR anomalies (W m^{-2}) during summer MHW events in the PRE. All anomalies are relative to the summer climatology over the corresponding analysis period. White rectangles mark the focal study regions.

https://doi.org/10.5194/egusphere-2026-3353
Preprint. Discussion started: 7 July 2026

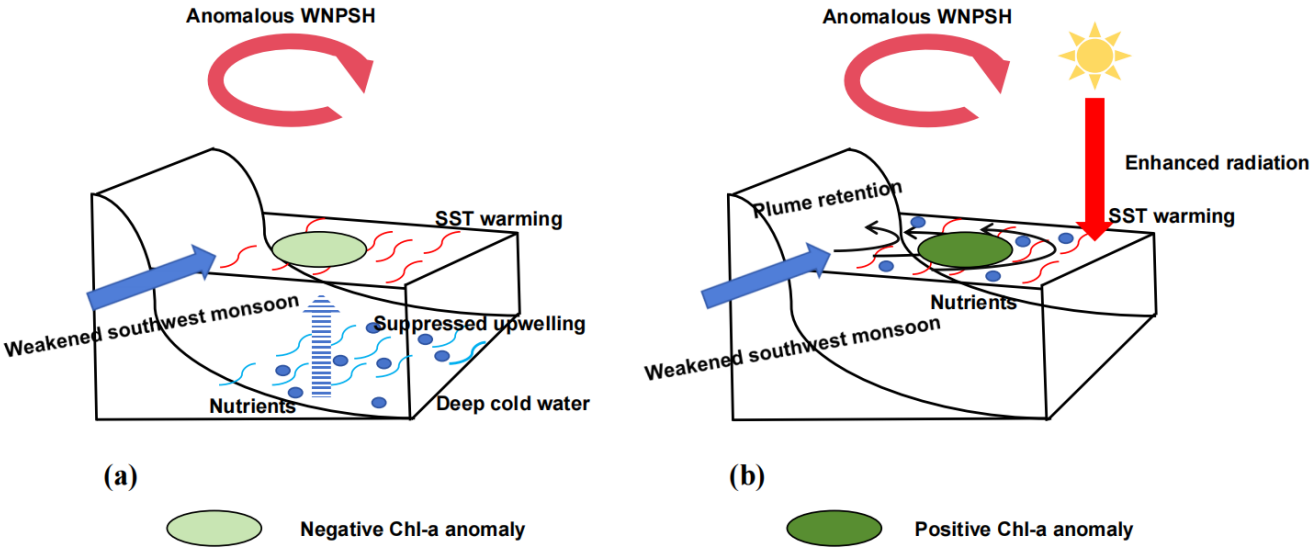

Figure 11. Schematic diagram of the contrasting physical–biological coupling mechanisms in the VUA and the PRE during summer MHWs under an anomalous WNPSH. (a) In the VUA, a weakened southwest monsoon suppresses coastal upwelling, which simultaneously reduces surface cooling and restricts subsurface nutrient supply, thereby favouring MHW development and a negative Chl-a anomaly. (b) In the PRE, enhanced shortwave radiation heats the surface water, while weakened wind-driven offshore transport promotes the nearshore retention of nutrient-rich river plumes, thereby favouring MHW development and a positive Chl-a anomaly. Arrows indicate key physical processes, and ellipse colours denote the sign of the Chl-a response.

4.3 Causal leakage and uncertainty in SURD-based interpretation

In the SURD framework, the causality leak represents the residual uncertainty of the target variable that cannot be explained by the selected driver set under the prescribed time lag, variable combination, and discretization scheme. It should not be interpreted as model failure, but rather as the incompleteness of the current variable set in explaining Chl-a variability. The causality leak is lower in the VUA than in the PRE, indicating that the selected physical variables capture a larger fraction of the information associated with Chl-a anomalies in the upwelling system, whereas greater unresolved uncertainty remains in the estuarine shelf system.

This regional difference reflects the contrasting process complexity of the two systems. In the VUA, negative Chl-a anomalies are closely linked to wind-driven vertical dynamics. The selected variables, including EPV, SSS, SLA, and SST_CUM, represent key physical processes such as weakened upwelling, thermocline adjustment, and enhanced stratification. The SURD decomposition thus provides a physically consistent interpretation of the Chl-a decline in the VUA. In comparison, the PRE is more complex. Chl-a variability there is influenced by wind-regulated plume retention and surface warming, but it is also modulated by biological processes, which are difficult to resolve using the current multi-source datasets, particularly sediment-driven light limitation and zooplankton grazing pressure (Chen et al., 2009; Lu and Gan, 2015). These processes were not included as SURD inputs and are therefore absorbed into the causality leak term.

https://doi.org/10.5194/egusphere-2026-3353
Preprint. Discussion started: 7 July 2026

Given these constraints, the PRE results should be interpreted as relative information contributions among the included physical variables, rather than as a complete attribution of estuarine Chl-a variability. The high unique contribution of SSS and the synergistic contribution among SST_CUM, SSS, SLA, and u_wind support a physically consistent plume-retention interpretation, but they are insufficient to establish the nutrient delivery pathway. The lag sensitivity tests and bin-based parameter selection support the robustness of the main SURD results. These tests cannot eliminate uncertainty arising from unresolved biological processes. Direct validation will require high-frequency in situ observations of nutrients, light attenuation, and plankton biomass during MHW events in the PRE.

5 Conclusions

This study used satellite observations and reanalysis data from 1998 to 2024 to investigate Chl-a responses to MHWs in the SCS. MHW metrics indicated prominent MHW activity in both the PRE and the VUA. During summer MHWs, Chl-a exhibited positive anomalies in the PRE and negative anomalies in the VUA. By applying SURD, we quantified the contributions of multiple physical drivers to these contrasting summer Chl-a responses.

Although WNPSH-related circulation anomalies provided a similar large-scale atmospheric background, the contrasting Chl-a responses were shaped largely by region-specific physical pathways. Direct thermal forcing alone was insufficient to explain these differences. In the VUA, the dominant unique contribution of EPV indicates that weakened upwelling was the key physical pathway linking MHW development and negative Chl-a anomalies. Reduced vertical transport restricted nutrient replenishment to the euphotic zone. In addition, weakened upwelling brought less cold subsurface water to the surface, enhancing the stratification during MHWs and thereby inhibiting vertical nutrient exchange. This process also contributed to the decline of the local Chl-a. In the PRE, the dominant unique contribution of SSS and its synergy with SST_CUM, SLA, and u_wind support a coupled radiative-warming and plume-retention interpretation. Enhanced shortwave radiation favoured rapid surface warming and MHW development in this shallow shelf region, while weakened wind-driven export promoted the nearshore retention of low-salinity plume water. The retained plume water strengthened upper-ocean stratification and likely enhanced nutrient availability, favouring for Chl-a accumulation within the euphotic zone.

By separating unique, redundant, and synergistic information, SURD distinguishes independent physical contributions from shared and joint effects among covarying drivers. The interpretation is limited by the variables in the current multi-source datasets, especially in the PRE. The higher causality leak in the PRE indicates that unresolved optical and biological processes, such as sediment-driven light limitation and zooplankton grazing, remain important sources of uncertainty. The plume-retention pathway in the PRE should therefore be treated as a physically supported interpretation rather than a complete explanation of the estuarine Chl-a response. Future high-frequency observations of nutrient, optical, and plankton observations will be needed to validate the inferred pathways.

Overall, this study shows that contrasting Chl-a responses to summer MHWs in the SCS cannot be explained by heat stress alone. In both the VUA and the PRE, heat accumulation acted mainly through joint effects with region-specific physical

https://doi.org/10.5194/egusphere-2026-3353
Preprint. Discussion started: 7 July 2026

processes rather than as the dominant independent driver. These findings help clarify why Chl-a responses differ among SCS regions and provide a more process-based view of physical–biological coupling during MHWs. Future applications of this SURD-based framework to other marginal seas, such as the Bohai Sea, Yellow Sea, and East China Sea, could help assess whether MHW-driven Chl-a responses arise from similar or regionally distinct physical–biological pathways.

Data availability

The datasets used in this study are publicly available from their respective data providers. SST data were downloaded from NOAA OISST v2.1 (https://www.ncei.noaa.gov/data/sea-surface-temperature-optimum-interpolation/v2.1/access/avhrr/, last access: 23 May 2026). Chl-a data were obtained from the Copernicus Marine Service GlobColour L4 product (https://data.marine.copernicus.eu/product/OCEANCOLOUR_GLO_BGC_L4_MY_009_104/services, last access: 23 May 2026). Salinity, temperature, currents, and MLD data were obtained from the Copernicus Marine Service GLORYS12V1 ocean reanalysis product (https://data.marine.copernicus.eu/product/GLOBAL_MULTIYEAR_PHY_001_030/services, last access: 23 May 2026). SLA data were obtained from the Copernicus Marine Service sea level product (https://data.marine.copernicus.eu/product/SEALEVEL_GLO_PHY_CLIMATE_L4_MY_008_057/services, last access: 23 May 2026). The 10 m wind and SWR data were obtained from ERA5 daily statistics on single levels (https://cds.climate.copernicus.eu/datasets/derived-era5-single-levels-daily-statistics?tab=download, last access: 23 May 2026). GH500 and 850 hPa wind data were obtained from ERA5 daily statistics on pressure levels (https://cds.climate.copernicus.eu/datasets/derived-era5-pressure-levels-daily-statistics?tab=download, last access: 23 May 2026). All datasets were used for the common analysis period of 1998–2024.

Author contributions

YLF and LC conceived the study. YLF, LC, and CYC designed the analysis framework. YLF compiled and processed the datasets, conducted the analyses, generated the figures, and wrote the original manuscript. CYC and MYL contributed to dataset compilation and checked the analyses. LC, CYC, and PLL contributed to the analysis design and interpretation of the results. All authors reviewed and edited the final version of the manuscript.

Competing interests

The contact author has declared that none of the authors has any competing interests.

https://doi.org/10.5194/egusphere-2026-3353
Preprint. Discussion started: 7 July 2026

Acknowledgements

The authors are grateful for the support provided by the Hainan Provincial Observatory of Ecological Environment and Fishery Resource in Yazhou Bay. The authors also acknowledge NOAA/NCEI, the Copernicus Marine Service, the Copernicus Climate Data Store, and ECMWF for providing the datasets used in this study.

Financial support

This research has been supported by the Project of Sanya Yazhou Bay Science and Technology City (contract no. SKJC-JYRC-2025-52), the Key Research and Development Program of Hainan Province (grant no. ZDYF2026SXLH039), and the Funds for Special Projects of the Central Government in Guidance of Local Science and Technology Development (grant no. 2025ZY01111).

References

Aurin, D. A. and Dierssen, H. M.: Advantages and limitations of ocean color remote sensing in CDOM-dominated, mineral-rich coastal and estuarine waters, Remote Sens. Environ., 125, 181–197, https://doi.org/10.1016/j.rse.2012.07.001, 2012.

Basconcillo, J. and Moon, I.-J.: Increasing activity of tropical cyclones in East Asia during the mature boreal autumn linked to long-term climate variability, npj Clim. Atmos. Sci., 5, 4, https://doi.org/10.1038/s41612-021-00222-6, 2022.

Cavole, L. M., Demko, A. M., Diner, R. E., Giddings, A., Koester, I., Pagniello, C. M. L. S., Paulsen, M.-L., Ramirez-Valdez, A., Schwenck, S. M., Yen, N. K., Zill, M. E., and Franks, P. J. S.: Biological impacts of the 2013–2015 warm-water anomaly in the Northeast Pacific: winners, losers, and the future, Oceanography, 29, 273–285, https://doi.org/10.5670/oceanog.2016.32, 2016.

Chen, B., Liu, H., Landry, M. R., Chen, M., Sun, J., Shek, L., Chen, X., and Harrison, P. J.: Estuarine nutrient loading affects phytoplankton growth and microzooplankton grazing at two contrasting sites in Hong Kong coastal waters, Mar. Ecol. Prog. Ser., 379, 77–90, https://doi.org/10.3354/meps07888, 2009.

Chen, Y., Shi, H., and Zhao, H.: Summer phytoplankton blooms induced by upwelling in the western South China Sea, Front. Mar. Sci., 8, 740130, https://doi.org/10.3389/fmars.2021.740130, 2021.

Chen, Y., Shen, C., Zhao, H., and Pan, G.: The impact of marine heatwaves on surface phytoplankton chlorophyll-a in the South China Sea, Sci. Total Environ., 949, 175099, https://doi.org/10.1016/j.scitotenv.2024.175099, 2024.

Chen, Z., Wang, Y., Wang, J., Zhang, R.-H., Jiang, Y., Qi, Y., and Yu, X.: Distinct mechanisms of marine heatwave formation in offshore waters of China, J. Oceanol. Limnol., 43, 1405–1424, https://doi.org/10.1007/s00343-025-4192-3, 2025.

Cheng, L., Abraham, J., Hausfather, Z., and Trenberth, K. E.: How fast are the oceans warming?, Science, 363, 128–129, https://doi.org/10.1126/science.aav7619, 2019.

https://doi.org/10.5194/egusphere-2026-3353
Preprint. Discussion started: 7 July 2026

Dai, M., Wang, L., Guo, X., Zhai, W., Li, Q., He, B., and Kao, S.-J.: Nitrification and inorganic nitrogen distribution in a large perturbed river/estuarine system: the Pearl River Estuary, China, Biogeosciences, 5, 1227–1244, https://doi.org/10.5194/bg-5-1227-2008, 2008.

Dippner, J. W., Nguyen, K. V., Hein, H., Ohde, T., and Loick, N.: Monsoon-induced upwelling off the Vietnamese coast, Ocean Dyn., 57, 46–62, https://doi.org/10.1007/s10236-006-0091-0, 2007.

Fernández-González, C., Tarran, G. A., Schuback, N., Woodward, E. M. S., Arístegui, J., and Marañón, E.: Phytoplankton responses to changing temperature and nutrient availability are consistent across the tropical and subtropical Atlantic, Commun. Biol., 5, 1035, https://doi.org/10.1038/s42003-022-03971-z, 2022.

Gao, Z., Jia, W., Zhang, W., and Wang, P.: Study on seasonal characteristics and causes of marine heatwaves in the South China Sea over nearly 30 years, Atmosphere, 14, 1822, https://doi.org/10.3390/atmos14121822, 2023.

Global Ocean Colour: Global Ocean Colour (Copernicus-GlobColour), Bio-Geo-Chemical, L4 (monthly and interpolated) from Satellite Observations (1997–ongoing), E.U. Copernicus Marine Service Information (CMEMS), Marine Data Store (MDS) [data set], https://doi.org/10.48670/moi-00281, 2025.

Global Ocean Gridded: Global Ocean Gridded L4 sea surface heights and derived variables reprocessed Copernicus Climate Service, E.U. Copernicus Marine Service Information (CMEMS), Marine Data Store (MDS) [data set], https://doi.org/10.48670/moi-00145, 2024.

Global Ocean Physics Reanalysis: Global Ocean Physics Reanalysis, E.U. Copernicus Marine Service Information (CMEMS), Marine Data Store (MDS) [data set], https://doi.org/10.48670/moi-00021, 2023.

Han, Y., Zhou, P., Lv, Q., Cui, R., and Meng, L.: Synergistic drivers and threshold effects of vapor pressure deficit in China: An integrated framework of causal inference and machine learning, J. Environ. Manag., 395, 127739, https://doi.org/10.1016/j.jenvman.2025.127739, 2025.

Harrison, P. J., Yin, K., Lee, J. H. W., Gan, J., and Liu, H.: Physical–biological coupling in the Pearl River Estuary, Cont. Shelf Res., 28, 1405–1415, https://doi.org/10.1016/j.csr.2007.02.011, 2008.

Hayashida, H., Matear, R. J., and Strutton, P. G.: Background nutrient concentration determines phytoplankton bloom response to marine heatwaves, Glob. Change Biol., 26, 4800–4811, https://doi.org/10.1111/gcb.15255, 2020.

He, J. and Mahadevan, A.: How the source depth of coastal upwelling relates to stratification and wind, J. Geophys. Res.-Oceans, 126, e2021JC017621, https://doi.org/10.1029/2021JC017621, 2021.

He, W., Zeng, X., Deng, L., Pi, Q. L. C., and Zhao, J.: Enhanced impact of prolonged MHWs on satellite-observed chlorophyll in the South China Sea, Prog. Oceanogr., 218, 103123, https://doi.org/10.1016/j.pocean.2023.103123, 2023.

Herrmann, M., To Duy, T., and Estournel, C.: Intraseasonal variability of the South Vietnam upwelling, South China Sea: influence of atmospheric forcing and ocean intrinsic variability, Ocean Sci., 19, 453–467, https://doi.org/10.5194/os-19-453-2023, 2023.

Hersbach, H., Comyn-Platt, E., Bell, B., Berrisford, P., Biavati, G., Horányi, A., Muñoz Sabater, J., Nicolas, J., Peubey, C., Radu, R., Rozum, I., Schepers, D., Simmons, A., Soci, C., Dee, D., Thépaut, J.-N., Cagnazo, C., and Cucchi, M.: ERA5 post-

https://doi.org/10.5194/egusphere-2026-3353
Preprint. Discussion started: 7 July 2026

519 processed daily statistics on pressure levels from 1940 to present, Copernicus Climate Change Service (C3S) Climate Data
520 Store (CDS) [data set], https://doi.org/10.24381/cds.50314f4c, 2023a.
521 Hersbach, H., Comyn-Platt, E., Bell, B., Berrisford, P., Biavati, G., Horányi, A., Muñoz Sabater, J., Nicolas, J., Peubey, C.,
522 Radu, R., Rozum, I., Schepers, D., Simmons, A., Soci, C., Dee, D., Thépaut, J.-N., Cagnazo, C., and Cucchi, M.: ERA5 post-
523 processed daily statistics on single levels from 1940 to present, Copernicus Climate Change Service (C3S) Climate Data Store
524 (CDS) [data set], https://doi.org/10.24381/cds.4991cf48, 2023b.
525 Hobday, A. J., Alexander, L. V., Perkins, S. E., Smale, D. A., Straub, S. C., Oliver, E. C. J., Benthuysen, J. A., Burrows, M.
526 T., Donat, M. G., Feng, M., Holbrook, N. J., Moore, P. J., Scannell, H. A., Sen Gupta, A., and Wernberg, T.: A hierarchical
527 approach to defining marine heatwaves, Prog. Oceanogr., 141, 227–238, https://doi.org/10.1016/j.pocean.2015.12.014, 2016.
528 Hong, B., Xue, H., Zhu, L., and Xu, H.: Climatic change of summer wind direction and its impact on hydrodynamic circulation
529 in the Pearl River Estuary, J. Mar. Sci. Eng., 10, 842, https://doi.org/10.3390/jmse10070842, 2022.
530 Huang, B., Liu, C., Banzon, V. F., Freeman, E., Graham, G., Hankins, W., Smith, T. M., and Zhang, H.-M.: NOAA 0.25-
531 degree Daily Optimum Interpolation Sea Surface Temperature (OISST), Version 2.1, NOAA National Centers for
532 Environmental Information [data set], https://doi.org/10.25921/RE9P-PT57, 2020.
533 Jiang, K., Wang, Y., Sun, Y., and Lan, J.: The seasonal variation of shallow meridional overturning circulation in the South
534 China Sea and the related dynamics, Ocean Model., 186, 102242, https://doi.org/10.1016/j.ocemod.2023.102242, 2023.
535 Jones, T., Parrish, J. K., Peterson, W. T., Bjorkstedt, E. P., Bond, N. A., Ballance, L. T., Bowes, V., Hipfner, J. M., Burgess,
536 H. K., Dolliver, J. E., Lindquist, K., Lindsey, J., Nevins, H. M., Robertson, R. R., Roletto, J., Wilson, L., Joyce, T., and Harvey,
537 J.: Massive mortality of a planktivorous seabird in response to a marine heatwave, Geophys. Res. Lett., 45, 3193–3202,
538 https://doi.org/10.1002/2017GL076164, 2018.
539 Le Grix, N., Zscheischler, J., Laufkötter, C., Rousseaux, C. S., and Frölicher, T. L.: Compound high-temperature and low-
540 chlorophyll extremes in the ocean over the satellite period, Biogeosciences, 18, 2119–2137, https://doi.org/10.5194/bg-18-
541 2119-2021, 2021.
542 Le Nohaïc, M., Ross, C. L., Cornwall, C. E., Comeau, S., Lowe, R., McCulloch, M. T., and Schoepf, V.: Marine heatwave
543 causes unprecedented regional mass bleaching of thermally resistant corals in northwestern Australia, Sci. Rep., 7, 14999,
544 https://doi.org/10.1038/s41598-017-14794-y, 2017.
545 Lellouche, J.-M., Greiner, E., Bourdallé-Badie, R., Garric, G., Melet, A., Drévillon, M., Bricaud, C., Hamon, M., Le Galloudec,
546 O., Regnier, C., Candela, T., Testut, C.-E., Gasparin, F., Ruggiero, G., Benkiran, M., Drillet, Y., and Le Traon, P.-Y.: The
547 Copernicus Global 1/12° oceanic and sea ice GLORYS12 reanalysis, Front. Earth Sci., 9, 698876,
548 https://doi.org/10.3389/feart.2021.698876, 2021.
549 Li, S., Yu, K., Chen, T., Shi, Q., and Zhang, H.: Assessment of coral bleaching using symbiotic zooxanthellae density and
550 satellite remote sensing data in the Nansha Islands, South China Sea, Chin. Sci. Bull., 56, 1031–1037,
551 https://doi.org/10.1007/s11434-011-4390-6, 2011.

https://doi.org/10.5194/egusphere-2026-3353
Preprint. Discussion started: 7 July 2026

Li, Y., Ren, G., Wang, Q., and You, Q.: More extreme marine heatwaves in the China Seas during the global warming hiatus, Environ. Res. Lett., 14, 104010, https://doi.org/10.1088/1748-9326/ab28bc, 2019.

Li, Y., Ren, G., Wang, Q., Mu, L., and Niu, Q.: Marine heatwaves in the South China Sea: tempo-spatial pattern and its association with large-scale circulation, Remote Sens., 14, 5829, https://doi.org/10.3390/rs14225829, 2022.

Liu, F. and Tang, S.: A double-peak intraseasonal pattern in the chlorophyll concentration associated with summer upwelling and mesoscale eddies in the western South China Sea, J. Geophys. Res.-Oceans, 127, e2021JC017402, https://doi.org/10.1029/2021JC017402, 2022.

Liu, W. T. and Xie, X.: Spacebased observations of the seasonal changes of south Asian monsoons and oceanic responses, Geophys. Res. Lett., 26, 1473–1476, https://doi.org/10.1029/1999GL900289, 1999.

Lu, Z. and Gan, J.: Controls of seasonal variability of phytoplankton blooms in the Pearl River Estuary, Deep-Sea Res. II: Top. Stud. Oceanogr., 117, 86–96, https://doi.org/10.1016/j.dsr2.2013.12.011, 2015.

Ma, X. and Chen, G.: Marine heatwaves are shaping the vertical structure of phytoplankton in the global ocean, Commun. Earth Environ., 6, 715, https://doi.org/10.1038/s43247-025-02718-y, 2025.

Mamnun, N. M. N., Völker, C., Vrekoussis, M., and Nerger, L.: Uncertainties in ocean biogeochemical simulations: Application of ensemble data assimilation to a one-dimensional model, Front. Mar. Sci., 9, 984236, https://doi.org/10.3389/fmars.2022.984236, 2022.

Marañón, E., Lorenzo, M. P., Cermeño, P., and Mouriño-Carballido, B.: Nutrient limitation suppresses the temperature dependence of phytoplankton metabolic rates, ISME J., 12, 1836–1845, https://doi.org/10.1038/s41396-018-0105-1, 2018.

Martínez-Sánchez, Á., Arranz, G., and Lozano-Durán, A.: Decomposing causality into its synergistic, unique, and redundant components, Nat. Commun., 15, 9296, https://doi.org/10.1038/s41467-024-53373-4, 2024.

Montie, S., Thomsen, M. S., Rack, W., and Broady, P. A.: Extreme summer marine heatwaves increase chlorophyll *a* in the Southern Ocean, Antarct. Sci., 32, 508–509, https://doi.org/10.1017/S0954102020000401, 2020.

Ngo, M.-H. and Hsin, Y.-C.: Impacts of wind and current on the interannual variation of the summertime upwelling off southern Vietnam in the South China Sea, J. Geophys. Res.-Oceans, 126, e2020JC016892, https://doi.org/10.1029/2020JC016892, 2021.

Nie, J., Fang, J., Yang, X.-Q., and Huang, Q.: Subseasonal relationship between the zonal oscillation of the Western Pacific Subtropical High and the South Asia High, Clim. Dynam., 62, 7293–7308, https://doi.org/10.1007/s00382-024-07279-y, 2024.

Niu, L., van Gelder, P., Luo, X., Cai, H., Zhang, T., and Yang, Q.: Implications of nutrient enrichment and related environmental impacts in the Pearl River Estuary, China: characterizing the seasonal influence of riverine input, Water, 12, 3245, https://doi.org/10.3390/w12113245, 2020.

Noh, K. M., Lim, H.-G., and Kug, J.-S.: Global chlorophyll responses to marine heatwaves in satellite ocean color, Environ. Res. Lett., 17, 064034, https://doi.org/10.1088/1748-9326/ac70ec, 2022.

https://doi.org/10.5194/egusphere-2026-3353
Preprint. Discussion started: 7 July 2026

584 Oliver, E. C. J., Benthuysen, J. A., Bindoff, N. L., Hobday, A. J., Holbrook, N. J., Mundy, C. N., and Perkins-Kirkpatrick, S.
585 E.: The unprecedented 2015/16 Tasman Sea marine heatwave, Nat. Commun., 8, 16101,
586 https://doi.org/10.1038/ncomms16101, 2017.
587 Oliver, E. C. J., Donat, M. G., Burrows, M. T., Moore, P. J., Smale, D. A., Alexander, L. V., Benthuysen, J. A., Feng, M., Sen
588 Gupta, A., Hobday, A. J., Holbrook, N. J., Perkins-Kirkpatrick, S. E., Scannell, H. A., Straub, S. C., and Wernberg, T.: Longer
589 and more frequent marine heatwaves over the past century, Nat. Commun., 9, 1324, https://doi.org/10.1038/s41467-018-
590 03732-9, 2018.
591 Robinson, A., Lehmann, J., Barriopedro, D., Rahmstorf, S., and Coumou, D.: Increasing heat and rainfall extremes now far
592 outside the historical climate, npj Clim. Atmos. Sci., 4, 45, https://doi.org/10.1038/s41612-021-00202-w, 2021.
593 Skákala, J., Ford, D., Fowler, A., Lea, D., Martin, M. J., and Ciavatta, S.: How uncertain and observable are marine ecosystem
594 indicators in shelf seas?, Prog. Oceanogr., 224, 103249, https://doi.org/10.1016/j.pocean.2024.103249, 2024.
595 von Schuckmann, K., Cheng, L., Palmer, M. D., Hansen, J., Tassone, C., Aich, V., Adusumilli, S., Beltrami, H., Boyer, T.,
596 Cuesta-Valero, F. J., Desbruyères, D., Domingues, C., García-García, A., Gentine, P., Gilson, J., Gorfer, M., Haimberger, L.,
597 Ishii, M., Johnson, G. C., Killick, R., King, B. A., Kirchengast, G., Kolodziejczyk, N., Lyman, J., Marzeion, B., Mayer, M.,
598 Monier, M., Monselesan, D. P., Purkey, S., Roemmich, D., Schweiger, A., Seneviratne, S. I., Shepherd, A., Slater, D. A.,
599 Steiner, A. K., Straneo, F., Timmermans, M.-L., and Wijffels, S. E.: Heat stored in the Earth system: where does the energy
600 go?, Earth Syst. Sci. Data, 12, 2013–2041, https://doi.org/10.5194/essd-12-2013-2020, 2020.
601 To Duy, T., Herrmann, M., Estournel, C., Marsaleix, P., Duhaut, T., Bui Hong, L., and Trinh Bich, N.: The role of wind,
602 mesoscale dynamics, and coastal circulation in the interannual variability of the South Vietnam Upwelling, South China Sea
603 – answers from a high-resolution ocean model, Ocean Sci., 18, 1131–1161, https://doi.org/10.5194/os-18-1131-2022, 2022.
604 Wang, Q., Wang, Y., Sui, J., Zhou, W., and Li, D.: Effects of weak and strong winter currents on the thermal state of the South
605 China Sea, J. Clim., 34, 313–325, https://doi.org/10.1175/JCLI-D-19-0790.1, 2021.
606 Wang, Q., Zhang, B., Zeng, L., He, Y., Wu, Z., and Chen, J.: Properties and drivers of marine heat waves in the northern South
607 China Sea, J. Phys. Oceanogr., 52, 917–927, https://doi.org/10.1175/JPO-D-21-0236.1, 2022.
608 Wang, Y., Zhang, C., Tian, S., Chen, Q., Li, S., Zeng, J., Wei, Z., and Xie, S.: Seasonal cycle of marine heatwaves in the
609 northern South China Sea, Clim. Dynam., 61, 3367–3377, https://doi.org/10.1007/s00382-023-06747-1, 2023.
610 Wernberg, T., Bennett, S., Babcock, R. C., De Bettignies, T., Cure, K., Depczynski, M., Dufois, F., Fromont, J., Fulton, C. J.,
611 Hovey, R. K., Harvey, E. S., Holmes, T. H., Kendrick, G. A., Radford, B., Santana-Garcon, J., Saunders, B. J., Smale, D. A.,
612 Thomsen, M. S., Tuckett, C. A., Tuya, F., Vanderklift, M. A., and Wilson, S.: Climate-driven regime shift of a temperate
613 marine ecosystem, Science, 353, 169–172, https://doi.org/10.1126/science.aad8745, 2016.
614 Wilcoxon, F.: Individual comparisons by ranking methods, Biometrics Bulletin, 1, 80–83, https://doi.org/10.2307/3001968,
615 1945.
616 Wu, X., Yao, F., and Wang, D.: Interannual variability of the summer surface salinity in the southern South China Sea driven
617 by the summer monsoon, J. Geophys. Res.-Oceans, 130, e2025JC022399, https://doi.org/10.1029/2025JC022399, 2025.

https://doi.org/10.5194/egusphere-2026-3353
Preprint. Discussion started: 7 July 2026

618 Yao, Y. and Wang, C.: Variations in summer marine heatwaves in the South China Sea, J. Geophys. Res.-Oceans, 126,
619 e2021JC017792, https://doi.org/10.1029/2021JC017792, 2021.
620 Yao, Y., Wang, J., Yin, J., and Zou, X.: Marine heatwaves in China's marginal seas and adjacent offshore waters: past, present,
621 and future, J. Geophys. Res.-Oceans, 125, e2019JC015801, https://doi.org/10.1029/2019JC015801, 2020.
622 Ye, H., Yang, C., Tang, S., and Chen, C.: The phytoplankton variability in the Pearl River estuary based on VIIRS imagery,
623 Cont. Shelf Res., 207, 104228, https://doi.org/10.1016/j.csr.2020.104228, 2020.
624 Zhao, H. and Tang, D. L.: Effect of 1998 El Niño on the distribution of phytoplankton in the South China Sea, J. Geophys.
625 Res.-Oceans, 112, C02017, https://doi.org/10.1029/2006JC003536, 2007.
626 Zhao, Z. and Marin, M.: A MATLAB toolbox to detect and analyze marine heatwaves, J. Open Source Softw., 4, 1124,
627 https://doi.org/10.21105/joss.01124, 2019.
628 Zhi, H., Wu, H., Wu, J., Zhang, W., and Wang, Y.: River plume rooted on the sea floor: seasonal and spring-neap variability
629 of the Pearl River plume front, Front. Mar. Sci., 9, 791948, https://doi.org/10.3389/fmars.2022.791948, 2022.